Transworld Research Network
37/661 (2), Fort P.O., Trivandrum-695 023, Kerala, India

Recent Res. Devel. Chem. Physics, 4(2003): 633-658 ISBN: 81-7895-095-2

27 Absolute and convective instabilities in the one-dimensional Brusselator model with flow

P.V. Kuptsov[1], S.P. Kuznetsov[1], C. Knudsen[2] and E. Mosekilde[2]
[1]Institute of Radio Engineering and Electronics, Russian Academy of Science, Zelenaya 38 Saratov 410019, Russia; [2]Department of Physics, The Technical University of Denmark 2800 Kgs. Lyngby, Denmark

Abstract

Turing and Hopf bifurcations are well-known examples of instabilities in chemical reaction-diffusion systems. In combination with an open flow, the field of dynamic phenomena becomes much richer as absolute and convective instabilities interact with the spatial and temporal pattern formation. This area of research is presently attracting considerable interest, particularly since it was shown theoretically as well as experimentally that stationary patterns can arise even when the interacting species have similar diffusion constants. Our paper presents a review of some of the new dynamical phenomena that one can observe in reaction-diffusion system with open flows. This review is based on an analysis of the one-dimensional Ginzburg-Landau equation for a Brusselator model with flow. Absolute and convective instabilities in the infinite system are discussed

Correspondence/Reprint request: Dr. P.V. Kuptsov, Institute of Radio Engineering and Electronics, Russian Academy of Science, Zelenaya 38, Saratov 410019, Russia. E-mail: kupav@mail.ru

together with the significance of inflow perturbations. In particular we discuss the rigid excitation of stationary patterns in the presence of inhomogeneous inflow conditions and suggest an estimate for the frequency of the nonlinear global mode near the critical point in a system with homogeneous inflow conditions.

1. Introduction

Hopf and Turing instabilities belong to the fundamental set of symmetry breaking bifurcations that one can observe in chemical reaction-diffusion systems under far-from-equilibrium conditions [1–3].

By breaking the time translation symmetry, the Hopf bifurcation leads to self-sustained temporal oscillations in the concentrations of the reacting species. This type of instability has been known in chemistry since the seminal works of Belousov and Zhabotinsky [4]. Numerous other autocatalytic reactions have since been found to exhibit a similar oscillatory behavior, and experiments in continuously stirred reactors have shown how the regular oscillations can develop into deterministic chaos and other forms of complex dynamics [5–7]. In unstirred reactors, the oscillatory dynamical processes can produce a variety of different wave-like phenomena, including, in two and three dimensions, rotating spirals and so-called target waves [8, 9]. These phenomena have been shown to arise directly from the coupling of the local nonlinear chemical reactions with the diffusion of the involved species.

The Turing instability, on the other hand, by breaking the translational symmetry in space, produces stationary patterns with a wavelength that is determined by the reaction parameters and diffusion constants of the chemical species [10–16]. In one-dimensional systems the patterns take the form of a regular stripe structure. In two-dimensional systems, both stripes and hexagons can occur, and subsequent instabilities can lead to the formation of zig-zag structures or to stripe structures with a modulation of the interstripe distance [17]. For the Turing instability to arise, the system must involve a positive feedback mechanism, typically in the form of an autocatalytic process by which an activator species reinforces its own production. The pattern-formation is controlled by the production of an inhibitor species (or by substrate depletion), and the instability depends on the inhibitor exhibiting a significantly larger diffusion rate than the activator.

When an instability occurs in a system with an open flow there are essentially two ways in which a spatially localized perturbation can grow. For low flow rates, the perturbation can spread to both sides, upstream as well as downstream, and the amplitude will grow at all points of space. This is referred to as the case of absolute instability. When the flow rate is sufficiently large, however, the growing perturbation will be swept along with the flow, and asymptotically the amplitude decays towards zero at all fixed points in space. This is the case of a convective instability [18–25]. In a reference frame that moves with flow the transition between the two instabilities may be considered as a problem of velocity selection for a front of the propagating perturbation [26–30].

The combination of an open flow with a chemical reaction-diffusion system enriches the field of dynamic phenomena significantly. This area of research has recently attracted considerable attention [31-40], particularly since it was suggested [24] that stationary spatial structure can emerge in such systems, even when the interacting species have similar diffusion constants. The conditions that must be satisfied to realize such pattern experimentally are relatively simple [34]. At the same time, the combination of an open flow with a chemical reaction system is of interest in connection with industrial production processes.

For semi-infinite systems, the boundary condition at the inflow has a significant influence on the dynamics. The so-called nonlinear global (NG) mode arises when the inflow condition corresponds to the homogeneous steady state of the system [31, 32]. However, the frequency of the NG mode differs from the frequency observed under the same conditions in an unbounded system.

With an inhomogeneous inflow condition a new type of pattern formation exists that differs from the "classical" Turing mechanism [24, 33, 34]. This is referred to as a "flow-distributed oscillations" (FDO) [34, 35]. In the general case when different forms of pattern formation take place, they are referred to as "flow and diffusion distributed structures" (FDS) [36, 37].

The cubic Ginzburg-Landau (GL) equation is a generic and well-studied model for a large class of dynamical phenomena in nonlinear systems [41]. This equation provides an approximate description of spatially extended systems near a bifurcation threshold, [2, 3, 42, 43]. The purpose of the present paper is to discuss the formation of flow and diffusion distributed structures by means of the GL equation. We consider this equation for a "canonical" reaction-diffusion model, namely the one-dimensional Brusselator in which a constant flow is present [24]. The GL equation for the Hopf bifurcation has a complex form while for the Turing case the form is real.

Some of the considered phenomena have been published before. However, we believe that it is useful to review them here and compare their manifestations in the GL equation for the Turing and Hopf instabilities. Special emphasis is given to a discussion of the rigid excitation of stationary patterns that are found to appear in presence of an inhomogeneous inflow perturbation. We also provide an estimate of the frequency of the nonlinear global mode near the critical point.

The organization of the paper is as follows. In Sec. 2 we review the basic instabilities in the one-dimensional Brusselator with flow. Section 3 discuses the GL equation for the Brusselator at the Hopf and Turing thresholds. Section 4 provides a linear analysis of the transition from absolute to convective instability, and the equations for the critical flow rate and for the corresponding frequency and wave number are obtained. Section 5 is devoted to a study of the stationary patterns that emerge when an inhomogeneous perturbation is applied to the inflow. In this connection, the rigid excitation of patterns is discussed. In Sec. 6 we consider the fully developed time-periodic solutions, when the time dependence is eliminated and the spatial dynamics is described by a set of ordinary differential equations. Finally, Sec. 7 contains an overview of the obtained results, and the Appendix illustrates the procedure for derivation of the GL equation.

2. Instabilities in the one-dimensional Brusselator model with flow

As a concrete example for our analysis we consider the one-dimensional Brusselator. This is one of the first and most influential models of reaction diffusion

systems under far-from-equilibrium conditions. In the presence of advection, the model is specified by the following set of dimensionless equations [24].

$$\begin{aligned} \frac{\partial U}{\partial t} + v\frac{\partial U}{\partial x} &= A - (B+1)U + U^2V + \sigma\frac{\partial^2 U}{\partial x^2}, \\ \frac{\partial V}{\partial t} + v\frac{\partial V}{\partial x} &= BU - U^2V + \frac{\partial^2 V}{\partial x^2}. \end{aligned} \tag{1}$$

Here, U and V denote the dynamical variables, and $A > 0$ and $B > 0$ are control parameters. More precisely, U and V represent the concentrations of two reacting chemical species, and A and B are the feed concentrations of two other species. $0 < \sigma \leq 1$ is the ratio of the diffusion constants for U and V, and $v > 0$ is the flow rate. The flow is supposed to be directed from the left towards the right. The system (1) has a homogeneous steady state (U_S, V_S) given by the equations

$$U_S = A,\ V_S = B/A. \tag{2}$$

In the absence of a flow, two "classical" bifurcations, namely the Hopf and the Turing bifurcations, are observed in the Brusselator model [1]. The corresponding instability thresholds as defined from the linear stability analysis are

$$B = B_H \equiv 1 + A^2 \text{ and } B = B_T \equiv (1 + A\sqrt{\sigma})^2. \tag{3}$$

If $B_H < B_T$, then a Hopf bifurcation occurs at $B = B_H$, and one observes the development of spatially homogeneous temporal oscillations. The corresponding critical wave number and frequency are

$$k_H = 0 \text{ and } \omega_H = A. \tag{4}$$

For $B_T < B_H$ the point $B = B_T$ is the threshold of a Turing bifurcation that results in a spatially periodic structure. This instability can only aries if there is a significant difference between the diffusion rates of the components U and V and, hence, only emerges for $\sigma < 1$. If the advection is absent ($v = 0$), the Turing structure is stationary. With a non-zero flow rate, on the other hand, temporal oscillations appear via the Doppler effect. At the critical point the structure is characterized by the wave number and the frequency:

$$k_T = \pm A^{1/2}\sigma^{-1/4} \text{ and } \omega_T = vk_T. \tag{5}$$

For reaction-diffusion-advection systems with a constant inflow perturbation the formation of stationary space periodic structures was recently predicted theoretically and soon after observed experimentally [34]. Such structures are now referred to as a flow-distributed oscillations (FDO) [34, 35]. FDO emerge in the Hopf instability domain, and the whole phenomenon is a remarkable example of a non-Turing mechanism of pattern formation. Moreover, this type of pattern formation happens even for equal diffusion coefficients.

The general situation where the stationary structures arises due to the combined action of flow and diffusion was discussed in a couple of recent papers by Satnoianu et al. [36, 37]. These structures are sometimes referred to as flow and diffusion distributed structures (FDS). FDS are shown to be more easily attainable in chemical systems than Turing (and FDO) structures and, hence, they may play an important role in biological pattern formation.

3. Ginzburg-Landau equation

For a wide class of systems near the bifurcation threshold the GL equation takes the form:

$$\partial_t w = p w - v\,\partial_x w + (b_1 + ic_1)\partial_x^2 w - (b_3 + ic_3)|w|^2 w \tag{6}$$

Here $w \equiv w(x, t)$ denotes the amplitude to be determined and p is the parameter that controls the distance from the bifurcation point. The remaining parameters b_1, c_1, b_3, and c_3 depend on the system under consideration.

The procedure for derivation of the coefficients of the GL equation is well-known, [2, 3, 42, 43]. For the considered reaction-diffusion system with flow the procedure is illustrated in the Appendix.

Near the Hopf threshold the coefficients for the system are:

$$\begin{aligned} p &= \frac{B - B_{\mathrm{H}}}{2}, \\ b_1 &= \frac{1+\sigma}{2},\; c_1 = \frac{A(1-\sigma)}{2}, \\ b_3 &= \frac{2 + A^2}{2A^2},\; c_3 = \frac{4 - 7A^2 + 4A^4}{6A^3}. \end{aligned} \tag{7}$$

Thus, in this case the GL equation (6) is complex. The coefficients b_1, c_1, b_3 and c_3 are always positive for the considered values of the parameters. (It can be shown that $c_3 = 0$ only for imaginary values of A and $c_3 > 0$ for real positive A.) When, in the initial system (1), the diffusion coefficients for U and V coincide ($\sigma = 1$) one has $b_1 = 1$, $c_1 = 0$ and, hence, the linear part of the GL equation for the Hopf case becomes real.

For the Turing case the GL equation is real and the coefficients read:

$$\begin{aligned} p &= \frac{B - B_{\mathrm{T}}}{\sqrt{B_{\mathrm{T}}}(1-\sigma)}, \\ b_1 &= \frac{4\sigma}{\sqrt{B_{\mathrm{T}}}(1-\sigma)},\; c_1 = 0, \\ b_3 &= \frac{-8 + 38A\sqrt{\sigma} + 5A^2\sigma - 8A^3\sigma^{3/2}}{9A^3(1-\sigma)\sqrt{\sigma}},\; c_3 = 0. \end{aligned} \tag{8}$$

The coefficient b_1 is always positive while b_3 is positive for

$$(21 - \sqrt{313})/16 < A\sqrt{\sigma} < (21 + \sqrt{313})/16. \tag{9}$$

As can be checked numerically, the fully developed oscillations in the Brusselator model (1) outside of this band is more complicated then the usual Turing oscillations, and the solution to the corresponding GL equation diverges. When $\sigma = 1$ the coefficients p, b_1 and b_3 diverge and pattern formation via the Turing mechanism can not occur.

4. Linear analysis of absolute and convective instabilities

The linearized GL equation reads:

$$\partial_t w = p w - v\,\partial_x w + (b_1 + ic_1)\partial_x^2 w. \tag{10}$$

Decomposing the solution of Eq. (10) in terms of elementary waves e^{st+qx} one obtains the dispersion relation

$$d(s,q) = s - p + v q - (b_1 + ic_1)q^2 \quad (s = \gamma - i\omega,\; q = \theta + ik), \tag{11}$$

where ω denotes the frequency and k is the wave number. γ and θ are the time and space increments, respectively.

The system (10) is stable when, for any spatially stable mode $q = ik$, the time increment is negative, $\gamma < 0$. One can easily check that this is the case for $p < 0$. Above the bifurcation point, where $p > 0$, the system is unstable. Separating the real and imaginary parts of (10) while keeping $\theta = 0$ one finds the band of linearly unstable modes:

$$k^2 < p/b_1. \tag{12}$$

Depending on the flow rate v the instability may be absolute or convective. There are two basic approaches to determine the critical value v_{ca}, namely the pinch-point analysis, [18–22] and the marginal stability analysis, [26–30]. Both approaches result in the same equations:

$$d(s,q) = 0,\; \operatorname{Re} s(q) = 0,\; \frac{\partial d/\partial q}{\partial d/\partial s} = 0. \tag{13}$$

Thus, by solving the equations (13) for the GL equation (10), one has [45]:

$$v_{\mathrm{ca}} = 2\sqrt{p\,(b_1^2 + c_1^2)/b_1}, \tag{14}$$

$$\omega_{\mathrm{ca}} = -p\,c_1/b_1, \tag{15}$$

$$k_{\mathrm{ca}} = -c_1\sqrt{p/(b_1(b_1^2 + c_1^2))}. \tag{16}$$

Note that k_{ca} belongs to the band of the linearly unstable modes (12). The above equations correspond to the Hopf case, while for the Turing case one needs to set $c_1 = c_3 = 0$. This gives $\omega_{ca} = k_{ca} = 0$, i.e., the solution is homogeneous.

Equation (14) suggests that a transition from absolute to convective instability will take place when the flow rate changes while the other parameters remain fixed. Alternatively, the transition can be observed when p changes while the flow rate remains fixed [32]. In this case the corresponding critical value reads

$$p_{ca} = v^2 b_1/(4(b_1^2 + c_1^2)). \tag{17}$$

The system is convectively unstable for $0 < p < p_{ca}$ and absolutely unstable for $p > p_{ca}$.

To obtain numerical solutions to the partial differential equations (1) and (6) we use the semi-implicit Crank-Nicholson scheme. Typical time and space step values are about 0.1. The right boundary condition is free and the left condition is taken to be constant.

Figure 1 compares the absolute and convective instabilities in the Brusselator model (1) (left column) with the corresponding instabilities in the GL equation (6) (right column). Observe that the fronts of perturbation propagate with the same velocities for the two models. In the complex GL equation for the Hopf instability only the slow oscillations are observed while for the Turing case one sees the homogeneous solution.

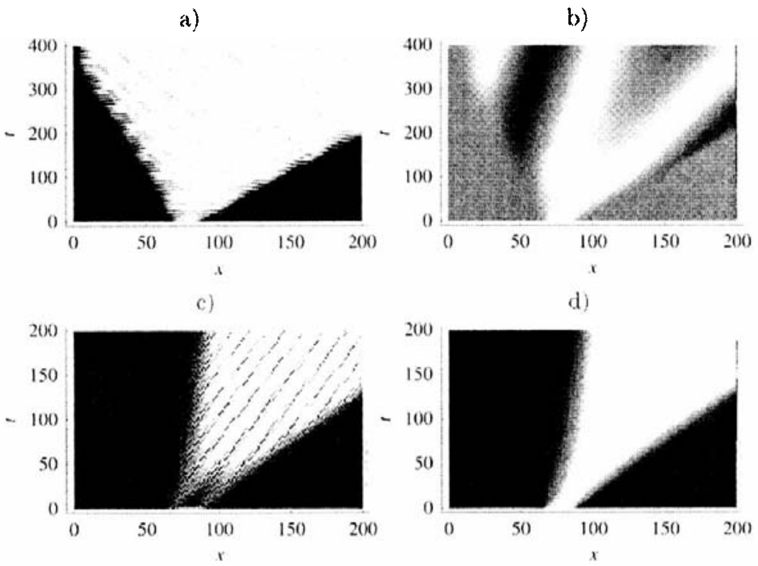

Figure 1. Absolute and convective instabilities in the Brusselator model (1) (panels (a) and (c)) and in the GL equation (6) (panels (b) and (d)). The coefficients to the GL equation were obtained from Eqs. (7) and (8). The gray scale represents U for the system (1) and Re w for the GL equation (6). Lighter tones correspond to larger values. Panels (a) and (b) represent the Hopf absolute instability at $A = 1$, $B = 2.1$, $\sigma = 0.25$, $v_{ca} = 0.412$. (c) and (d) show the Turing convective instability at $A = 2$, $B = 4.1$, $\sigma = 0.25$, $v_{ca} = 0.422$. The flow rate is $v = 0.2$ for panels (a) and (b), and $v = 0.5$ for (c) and (d).

5. Stationary patterns induced by the inflow perturbation

Spatially periodic, stationary patterns (flow and difusion distributed structures (FDS), [36, 37] are known to appear in reaction-diffusion systems with flow when a constant inhomogeneous boundary condition is applied to the system inlet [24, 33, 34] provided that the flow rate is larger then some critical value. Below we consider these structures for the Turing and Hopf GL equation (i.e., for the real and complex versions of the GL equation, respectively). As we shall see, a stationary pattern may be excited even below the critical flow rate, if the amplitude of perturbation is large enough. In this case a rigid excitation takes place.

It is important to recall here that the considered GL equation describes the slow modulation of the oscillating solution to the Brusselator (1) (see Appendix for details). This means that even if the solution to the GL equation is stationary, the corresponding solution to the original system is oscillating. Hence, relative to the original system (1) the stationary structures considered below may be treated as a "secondary" or "modulating" FDS.

Applying the inhomogeneous boundary condition $w_{x=0} \neq 0$ to the GL equation (6) one finds the threshold value for the flow rate by substituting $s = 0$ into the dispersion equation (11):

$$(b_1 + ic_1)q^2 - vq + p = 0. \tag{18}$$

This equation has two solutions, q_1 and q_2, that determine the wave numbers and amplitude increments towards the positive semi-space and in the backward direction, respectively. One obtains the critical flow rate by substituting $q = ik$ into (18) and separating the real and imaginary parts:

$$v_{st} = c_1\sqrt{p/b_1},\ k_{st} = -\sqrt{p/b_1}. \tag{19}$$

For $v < v_{st}$ the real parts of q_1 and q_2 have different signs, and they are both positive above this threshold. This means that the stationary pattern must grow towards the positive semi-space for $v > v_{st}$. However, as noted by Andresén et al. [33], the stationary pattern develops from the constant inflow perturbation if the flow rate is above both v_{ca} and v_{st}. One can easily check that for the considered case $v < v_{st}$ and, hence, the threshold value for the stationary pattern is v_{ca}, while v_{st} is the lower flow rate for which the stationary solution exists (but, possibly, without being selected). Note that k_{st} lies on the left boundary of the interval of the linearly unstable modes (12). In the following we shall show that the stationary solution can be selected even below the critical point v_{ca} if the inflow perturbation is large enough.

Let us first consider the Turing case. Because the coefficients of the corresponding GL equation are real, temporal oscillations are not observed, and the following stationary solutions exist:

$$W_L = 0,\ W_N^{\pm} = \pm\sqrt{p/b_3}. \tag{20}$$

The solutions W_N^+ and W_N^- are symmetrical about the unperturbed steady state W_L, and the system (6) selects one of them depending on the initial state. To observe growth of the stationary mode from the constant inflow boundary perturbation, we introduce a small negative fluctuations as the initial conditions for $t = 0$ and apply a small positive boundary condition at $x = 0$. This combination of boundary and initially conditions results in the competition of two modes, W_N^- and W_N^+ that is shown in Fig. 2(a). Here the black shading represents the W_N^- mode, white is W_N^+ and gray is W_L. As we can see, for flow rates above the critical point, $v > v_{ca}$, the mode W_N^+ initiated by the boundary perturbation dominates and spreads over the whole semi-space.

This is not in disagreement with the previously reported condition that FDS arises outside the Turing instability domain, [24, 33, 34, 36]. As noted above, the considered GL equation corresponds to the oscillating solution of the Brusselator (1) and, hence, the described effect in the original system (1) corresponds to a running phase flip between two modes with the same frequencies.

For the Hopf case a similar but more complicated picture is observed. This is illustrated in Fig. 2(b). Above the threshold v_{ca} the stationary mode develops from the boundary perturbation and all time oscillating structures drift downflow. This is a typical manifestation of FDS [24, 33, 34]. The presented figure corresponds to the case of different diffusion coefficients in the original system (1), i.e, $\sigma < 1$, but qualitatively the same situation has been observed for $\sigma = 1$.

Let us now consider flow rates below the critical value v_{ca}. In this case stationary structures are found to emerge when the boundary perturbation is large enough such that a rigid excitation can take place.

The rigid excitation for the Turing case is illustrated in Fig. 3. For this figure both the initial and boundary conditions are the same as in Fig. 2(a). The panels (a) and (b) are computed at $v > v_{ca}$ for the same parameters and initial conditions but with different

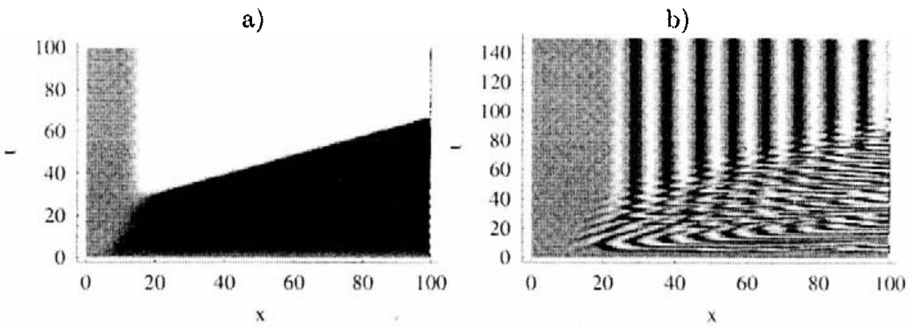

Figure 2. Stationary structure, emerging for the constant inflow perturbation (i.e. FDS) in the GL equation (6) for (a) Turing and (b) Hopf cases. The perturbation is $w|_{x=0}=10^{-4}$ for both cases, and the other parameters are: p=1, b_1=1, b_3=1, v=2.2 (v_{ca}=2), (b) p=1, b_1=1, c1=1, b_3=1, c3=3, v=3 (v_{ca}=2.828). In panel (a) for the Turing case the white tone corresponds to the positive homogeneous solution, the black represents the negative solution and the gray is the steady state. The initial conditions are small negative fluctuations while the inflow perturbation is positive.

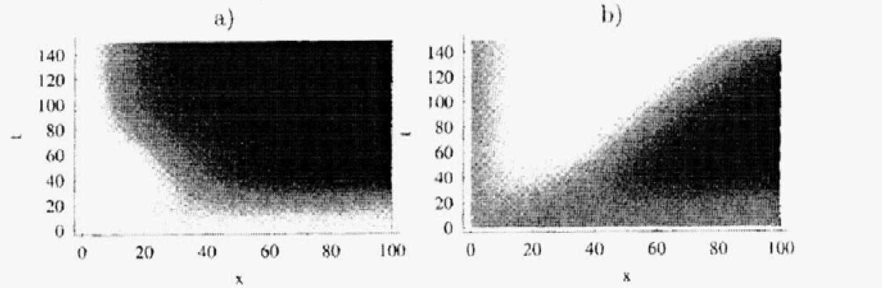

Figure 3. Rigid excitation of the homogeneous stationary structure by the constant inflow perturbation in the GL equation (6) for the Turing case. The parameters are: $p = 0.1$, $b_1 = 10$, $b_3 = 3$, and $v = 0.5$ ($v_{ca} = 2$). The initial conditions are small negative fluctuations with amplitude 0.005. In the panel (a) the inflow perturbation is too small, $w|_{x=0} = 0.02$, to induce a stationary structure, while in the panel (b) the homogeneous structure emerges for the larger perturbation $w|_{x=0} = 0.04$.

inflow perturbations. In panel (a) the perturbation is small and mode W_N^- grows from the initial state while the boundary perturbation decays. On the contrary, in panel (b) the larger boundary perturbation grows to the mode W_N^+ and the state W_N^- drifts downflow. The threshold value of the inflow perturbation depends on the amplitude of the initial perturbations and becomes larger for larger initial amplitudes.

The rigid excitation of flow and diffusion distributed structures in the Hopf case is illustrated in Fig. 4. In this figure $v < v_{ca}$ and all the panels are drawn for the same parameters. The boundary perturbation $w|_{x=0}$ increases from panel (a) to panel (d). Observe how the homogeneous boundary condition $w|_{x=0} = 0$ in panel (a) and a small inhomogeneous perturbation in panel (b) induce the oscillating modes. The mode in panel (a) is an NG mode as described by Couairon and Chomaz [32]. Note that the structure near the inlet in panel (b) has the same space and time periods as in panel (a) and that the presence of the boundary perturbation results in a failure of the wave propagation[1]. With further increase of $w|_{x=0}$ the oscillating mode disappears and a FDS emerges that is "weak" and decaying in panel (c), and spreading over the space in panel (d).

Note that in contrast to the Turing case, where two competing modes are excited by the initial and boundary perturbations respectively, for the Hopf case both the oscillating mode and the FDS are induced by the boundary perturbation and, hence, the qualitative picture does not depend on the amplitude of the initial perturbation.

As we can observe from the numerical simulation, the effect of rigid excitation of FDS is not specific to the GL equation. For the Brusselator model (1) in the Hopf instability domain when $v_{st} > v_{ca}$ no stationary structures exist below the threshold v_{st} for any inflow perturbation. But if $v_{st} < v_{ca}$, as for the GL equation, the rigid excitation

[1]As we have checked, this wave propagation failure is not a consequence of the right boundary. The same picture is observed even if the system is very long and the initial perturbation does not reach the right boundary during the observation.

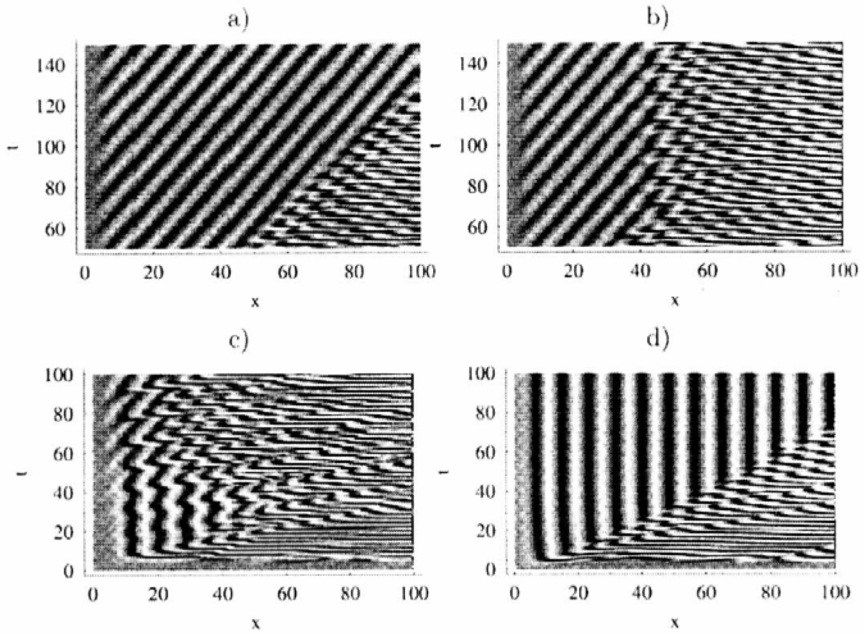

Figure 4. Rigid excitation of FDS in the GL equation (6) for the Hopf case when $v < v_{ca}$. For all panels the parameters are: $p = 1$, $b_1 = 1$, $c_1 = 1$, $b_3 = 1$, $c_3 = 3$, and $v = 2.5$ ($v_{ca} = 2.828$). No FDS exist when the inflow perturbation is absent as in panel (a), $w_{|x=0} = 0$, or is small as in panel (b), $w_{|x=0} = 0.001$. When the perturbation becomes larger, the "weak" FDS first disappears after some time as in panel (c), $w_{|x=0} = 0.01$, and then the FDS spreads in space as in panel (d), $w_{|x=0} = 0.05$. Observe that in panels (a) and (b) the wave states near the system inlet are the same, but the wave is not running downflow for the inhomogeneous perturbation in panel (b).

takes place. This is shown in Fig. 5. For both panels in this figure $v_{st} < v < v_{ca}$; in the panel (a) the small perturbation is too weak to induce a stationary structure while in panel (b) the perturbation is larger and a stationary structure appears.

6. Time periodic solutions

In this section we consider a class of solutions to the GL equation (6) that are time periodic for the Hopf case (i.e., for the complex GL equation) and stationary for the Turing case (when the GL equation is real). For this class of solutions the partial differential equation (6) reduces to a set of ordinary differential equations for an amplitude and phase of the solution. Fixed points of these equations are the nonlinear wave states of the GL equation and heteroclinic orbits, joining these points, are fronts, pulses, and other localized structures separating ideal patterns. This approach is one of the "classical" methods for analyzing the GL equation and has been utilized by many authors. Particularly, detailed analyses of the complex GL equation are provided by van Saarloos and Hohenberg [45]. Peculiarities of absolute and convective instabilities for

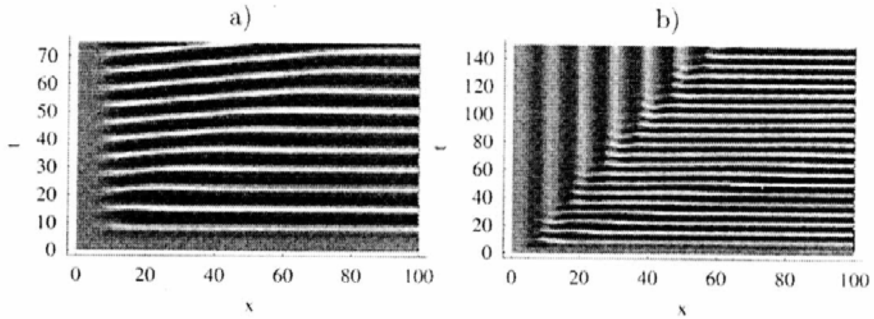

Figure 5. Rigid excitation of FDS in the Brusselator model with flow (1). The parameters are in Hopf instability domain: $A = 1$, $B = 3$, $\sigma = 0.6$, and $v = 1.2$ ($v_{st} = 0.851$ and $v_{ca} = 1.335$). Note that $v_{st} < v < v_{ca}$. Hopf oscillations exist in panel (a), where the inflow perturbation is small, $U_{|x=0} = U_S + 0.01$, and in panel (b) FDS appears for $U_{|x=0} = U_S + 0.1$. (Here U_S is the homogeneous steady state (2)).

nonlinear systems were considered by Chomaz [23] and by Couairon and Chomaz [31] using the real GL equation [31]. The NG modes appearing in the presence of a homogeneous inflow boundary condition were studied by Couairon and Chomaz both in the real GL equation and in the complex GL equation [32]. Below we briefly summarize the most important results for the Hopf and Turing instabilities and suggest an estimate for the frequency of the NG mode near the critical point. Finally, we discuss the rigid excitation of flow and diffusion distributed structures that was observed in Sec. 5.

Let the solution to the GL equation (6) be of the form:

$$w(x,t) = W(x)e^{i(kx-\omega t)}, \tag{21}$$

where $W(x)$ is a complex function of x, and k and ω are the real wave number and frequency, respectively. This form of solution is appropriate for the Hopf case while for the Turing case k and ω become equal to zero and $W(x)$ is real.

Often an ansatz for the structure of a time periodic solution different from (21) is used: $W(x)$ is supposed to be real and a real function of x is written instead of kx in (21) [32, 45]. This leads to a three-dimensional set of ordinary differential equations with a singularity in the phase space. On the other hand, the formulation (21) leads to a four-dimensional dynamical system without a singularity and, hence, as noted in [32], this formulation is more appropriate for numerical simulations. Below we present the results of these simulations. In particular, we discuss the structure of the phase space near the fixed points.

Let us suppose for a moment that W is constant and substitute (21) into the GL equation (6). We find that the nonzero amplitude W exists only if ω and k satisfy the equation

$$b_3\omega = c_3p + vb_3k + (c_1b_3 - c_3b_1)k^2, \tag{22}$$

and k belongs to the interval

$$k^2 < p/b_1. \tag{23}$$

For the Turing case $c_1 = c_3 = 0$, and Eq. (22) reduces to

$$\omega = vk. \tag{24}$$

Because we assume $\omega = k = 0$, this is always satisfied.

Equation (22) couples the values of ω and k for which the time periodic solution exists and, hence, plays the same role as the dispersion equation (11) for linear oscillations. Observe that the interval (23), where the solution exists, is the same as the interval (12) for the linearly unstable modes. Note that for the frequency ω we obtain different wave numbers k from Eq. (11) and Eq. (22). This is a manifestation of the well-known phenomenon that the period of oscillation in a nonlinear system depends on its amplitude.

Let us now find the equation for $W(x)$. Substituting Eq. (21) into the GL equation (6) and eliminating ω by using Eq. (22) we have for the Hopf case:

$$(b_0 + ic_0)\partial_x W - (b_1 + ic_1)\partial_x^2 W + (b_3 + ic_3)(|W|^2 - \chi^2)W = 0, \tag{25}$$

where the following notation is used:

$$\chi = \sqrt{(p - b_1k^2)/b_3},\ b_0 = v + 2c_1k,\ c_0 = -2b_1k. \tag{26}$$

For the Turing case $c_1 = c_3 = 0$, $k = 0$, hence

$$\chi = \sqrt{p/b_3},\ b_0 = v,\ c_0 = 0, \tag{27}$$

and Eq. (25) is real.

Equation (25) has the fixed points

$$W_{\rm L} = 0 \ \text{ and } \ |W_{\rm N}| = \chi. \tag{28}$$

Due to the phase invariance of the GL equation, $w \to w\, e^{i\phi}$, the $W_{\rm N}$ points form an invariant set that is a circle around $W_{\rm L}$ for the Hopf case and a pair of points in the Turing case.

Equation (25) may be transformed into a set of four real equations of first order by separating the real and imaginary parts of the complex amplitude $W(x) = U_0(x) + iV_0(x)$:

$$\begin{aligned}
\partial_x U_0 &= U_1,\\
\partial_x V_0 &= V_1,\\
\partial_x U_1 &= \tilde{b}_0 U_1 - \tilde{c}_0 V_1 + (\tilde{b}_3 U_0 - \tilde{c}_3 V_0)(U_0^2 + V_0^2 - \chi^2),\\
\partial_x V_1 &= \tilde{b}_0 V_1 + \tilde{c}_0 U_1 + (\tilde{b}_3 V_0 + \tilde{c}_3 U_0)(U_0^2 + V_0^2 - \chi^2).
\end{aligned} \tag{29}$$

In the Turing case the amplitude $W(x)$ is real and one has a set of two equations:

$$\begin{aligned}
\partial_x U_0 &= U_1,\\
\partial_x U_1 &= \tilde{b}_0 U_1 + \tilde{b}_3 U_0 (U_0^2 - \chi^2)
\end{aligned} \tag{30}$$

(here $W(x) = U_0(x)$). The coefficients for the Hopf case, Eqs. (29), are:

$$\begin{aligned}
\tilde{b}_0 &= \frac{b_1b_0 + c_1c_0}{b_1^2 + c_1^2}, & \tilde{c}_0 &= \frac{b_1c_0 - c_1b_0}{b_1^2 + c_1^2},\\
\tilde{b}_3 &= \frac{b_1b_3 + c_1c_3}{b_1^2 + c_1^2}, & \tilde{c}_3 &= \frac{b_1c_3 - c_1b_3}{b_1^2 + c_1^2},
\end{aligned} \tag{31}$$

We recall that the control parameter p is hidden in χ, that the flow rate v is present in b_0 and that the wave number k appears in χ, b_0, and c_0 (see (26)). The fixed points in terms of these equations are

$$\begin{aligned}
W_{\rm L} &= (U_0, V_0, U_1, V_1)_{\rm L} = (0, 0, 0, 0),\\
W_{\rm N} &= (U_0, V_0, U_1, V_1)_{\rm N} = (\chi\cos\phi, \chi\sin\phi, 0, 0),
\end{aligned} \tag{32}$$

where ϕ is an arbitrary phase. For the Turing case, Eq. (30), the coefficients (31) are reduced to

$$\tilde{b}_0 = v/b_1,\ \tilde{b}_3 = b_3/b_1, \tag{33}$$

and the fixed points are

$$W_{\rm L} = (0, 0) \ \text{ and } \ W_{\rm N} = (\pm\chi, 0). \tag{34}$$

Let us first discuss the Turing case where the considered equations are real. A more complicated case where the real GL equation includes higher order terms in w was studied by Chomaz at al. [23, 31]

Near the fixed points of Eq. (30) the dynamics is described by the matrixes:

$$\mathcal{L}_{\rm L} = \begin{pmatrix} 0 & 1 \\ -p/b_1 & v/b_1 \end{pmatrix},\ \mathcal{L}_{\rm N} = \begin{pmatrix} 0 & 1 \\ 2p/b_1 & v/b_1 \end{pmatrix}. \tag{35}$$

The corresponding eigenvalues are

$$\lambda_{\rm L1,2} = \frac{v \mp \sqrt{v^2 - 4pb_1}}{2b_1},\ \lambda_{\rm N1,2} = \frac{v \mp \sqrt{v^2 + 8pb_1}}{2b_1}. \tag{36}$$

Because $p > 0$ and $b_1 > 0$, the eigenvalues $\lambda_{L1,2}$ are real for large flow rates and becomes complex when v falls below the absolute instability threshold v_{ca} (14). Their real parts are always positive. Hence, W_L is a source for the absolute instability and an unstable node if the instability is convective. The eigenvalues $\lambda_{N1,2}$ are always real and have opposite signs, $\lambda_{N1} < 0$ and $\lambda_{N2} > 0$, such that both W_N points are saddles.

The fixed points are linked by the heteroclinic orbits that represent the moving front solution in the spatially unlimited system (6). To obtain such an orbit numerically, one needs to apply a small perturbation along the eigenvector corresponding to λ_{N1} to one of the points W_N and then solve the equations (30) with a negative discretization step. In Fig. 6 the heteroclinic orbits are drawn for the convective and absolute instabilities. These orbits leave W_L as unstable manifolds and approach W_N as stable manifolds.

In the semi-infinite system with a homogeneous boundary condition at the inlet, the nonlinear global mode develops. This is discussed by Couairon and Chomaz [31]. To represent the NG solution the heteroclinic orbit must cross the axes U_1 without passing through W_L, i.e, with some non-zero value U_1. One sees from Fig. 6 that such an orbit exists only when the instability is absolute.

For solutions to the system (6) with the non-homogeneous boundary condition $w_{x=0} = \rho$, the representing heteroclinic orbit must cross the vertical line $U_0 = \rho$. As seen from Fig. 6(a), in the convectively unstable system for any $|\rho| < \chi$ there is always one orbit that crosses this line, and the sign of ρ determines the mode, W_N^+ or W_N^- that the system selects. This situation is discussed in Sec. 5 and illustrated in Fig.2(a).

A different situation is observed for the absolute instability, as illustrated in Fig. 6(b). The heteroclinic orbits first leave the origin spiralling and then take the from of an arc. When ρ is inside the region of spiraling (this is marked in the figure by the vertical dashed lines) the condition of existence is satisfied both for mode W_N^+ and for mode W_N^-, because both of the corresponding orbits cross the line $U_0 = \rho$. The ordinates of these intersection points are the slopes at the origin of the corresponding solutions to the system (6). Thus, the system selects the solution depending on the slope of the initial distribution $w(x, t = 0)$. In particular, for positive ρ this means that if the initial

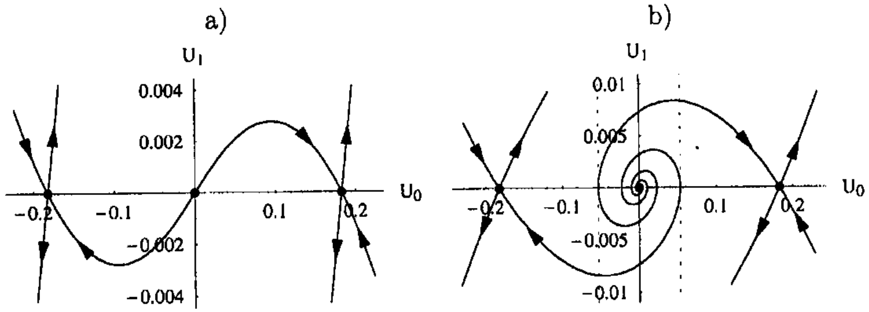

Figure 6. Heteroclinic orbits in the Turing case, Eq. (30), for parameters $p = 0.1$, $b_1 = 10$, $b_3 = 3$ ($v_{ca} = 2$) (same as in Fig 3). Instability is convective in panel (a), $v = 2.5$, and absolute in panel (b), $v = 0.5$. The dashed lines $U_0 \approx \pm 0.052$ in panel (b) mark the boundaries of spiralling.

perturbation is negative and large enough then the system selects the mode W_N^-, while for small negative perturbation the mode W_N^+ is selected. An example of this selection is discussed in Sec. 5 and shown in Fig. 3. For a large inflow perturbation ρ, that is outside the region of spiralling, the situation is the same as for the convective instability: Only one of the orbits crosses the line $U_0 = \rho$ and the corresponding solution is selected by the system.

Let us now turn to the Hopf case. In this case Eq. (21) defines the family of solutions to the GL equation parameterized by ω. One of these solutions is dynamically selected by the system. For the spatially infinite system the selection criteria are well studied, see [29, 30, 45] and references therein. As mentioned in Sec. 4, exactly at the point of transition from absolute to convective instability, i.e. at $v = v_{ca}$, the frequency ω is determined by Eq. (15). Substituting $v = v_{ca}$ and $\omega = \omega_{ca}$ into Eq. (22) and taking into account (23), one obtains the corresponding wave number:

$$k_{\rm inf} = \sqrt{\frac{p}{b_1}}\left(\frac{b_3\sqrt{b_1^2+c_1^2} - b_1\sqrt{b_3^2+c_3^2}}{b_1 c_3 - c_1 b_3}\right). \tag{37}$$

Supposing that the frequency depends linearly on v while the wave number is constant, one writes:

$$\omega_{\rm inf} = \omega_{\rm ca} + k_{\rm inf}(v - v_{\rm ca}). \tag{38}$$

The pair $k_{\rm inf}$ and $\omega_{\rm inf}$ satisfies Eq. (22) and, as can be checked numerically, agrees well the frequency and the wave number of fully developed oscillations in the spatially infinite system.

The dynamics of Eq. (29) linearized near the point W_L is described by the matrix

$$\mathcal{L}_L = \begin{pmatrix} 0 & 0 & 1 & 0 \\ 0 & 0 & 0 & 1 \\ -\tilde{b}_3\chi^2 & \tilde{c}_3\chi^2 & \tilde{b}_0 & -\tilde{c}_0 \\ -\tilde{c}_3\chi^2 & -\tilde{b}_3\chi^2 & \tilde{c}_0 & \tilde{b}_0 \end{pmatrix}. \tag{39}$$

The eigenvalues of $\mathcal{L}_L$ are:

$$\begin{aligned} \lambda_{L1} &= \frac{\tilde{b}_0 + i\tilde{c}_0}{2} - \frac{\sqrt{(\tilde{b}_0 + i\tilde{c}_0)^2 - 4\chi^2(\tilde{b}_3 + i\tilde{c}_3)}}{2}, \\ \lambda_{L2} &= \frac{\tilde{b}_0 + i\tilde{c}_0}{2} + \frac{\sqrt{(\tilde{b}_0 + i\tilde{c}_0)^2 - 4\chi^2(\tilde{b}_3 + i\tilde{c}_3)}}{2}, \\ \lambda_{L3} &= \overline{\lambda}_{L1}, \\ \lambda_{L4} &= \overline{\lambda}_{L2}, \end{aligned} \tag{40}$$

where an overbar denotes complex conjugation. To study the properties of these eigenvalues, one can represent the complex expression under the square roots in terms of their absolute value and phase and then find the real and imaginary parts of λ_L. In this way we obtain the following equations:

$$\mathrm{Re}\,\lambda_L = 0 \ \Rightarrow\ \chi^2(\tilde{b}_0^2\tilde{b}_3 + \tilde{b}_0\tilde{c}_0\tilde{c}_3 - \tilde{c}_3^2\chi^2) = 0, \tag{41}$$

$$\mathrm{Im}\,\lambda_L = 0 \ \Rightarrow\ \chi^2(\tilde{c}_0^2\tilde{b}_3 - \tilde{b}_0\tilde{c}_0\tilde{c}_3 + \tilde{c}_3^2\chi^2) = 0, \tag{42}$$

$$\mathrm{Re}\,(\lambda_{L1} - \lambda_{L2}) = 0 \ \Rightarrow\ \tilde{b}_0\tilde{c}_0 - 2\tilde{c}_3\chi^2 = 0 \ \text{ and } \ N \geq 0, \tag{43}$$

$$\mathrm{Im}\,(\lambda_{L1} - \lambda_{L2}) = 0 \ \Rightarrow\ \tilde{b}_0\tilde{c}_0 - 2\tilde{c}_3\chi^2 = 0 \ \text{ and } \ N \leq 0, \tag{44}$$

where $N = \tilde{b}_0^2 + 4\tilde{b}_3\chi^2 - 4\tilde{c}_3^2\chi^4/\tilde{c}_0^2$. If k lies on the boundary of interval of permitted values (23), then $\chi = 0$, see Eq. (26) and, hence, two of the eigenvalues are zero. For the spatially infinite system in the critical point $k = k_{\text{inf}}$ and $v = v_{\text{ca}}$. In this case $N = 0$, and both the equations (43) and (44) are satisfied. Hence $\lambda_{L1} = \lambda_{L2}$ and $\lambda_{L3} = \lambda_{L4}$. Note that this is similar to the Turing case. The condition $\mathrm{Im}\,\lambda_L = 0$ is satisfied only for some definite values of v, and the eigenvalues are complex pairs both for the case of convective and for the absolute instability. This represents an important difference relative to the Turing case, where the corresponding eigenvalues (36) are real for the convective instability and complex when the instability is absolute.

The fixed points of Eq. (29) fill the invariant circle in the phase space and, hence, there exists a set of the heteroclinic orbits corresponding to each point of this circle. Because of their obvious identical dynamical properties, one can consider only one representative of this set. In Fig. 7(a) and (b) the heteroclinic orbits for the point $W_N^+ = \chi$ are drawn that correspond to the convective and absolute instability in the spatially infinite system (6). One sees no qualitative difference in comparison with the Turing case in Fig. 6. In Fig. 8 the roots of Eqs. (41)-(44) are plotted in the plane (k, v). All the eigenvalues have positive real parts above the line $\mathrm{Re}\,\lambda_L = 0$, and the real parts for two of them are negative below this line. The vertical line $k = k_{\text{inf}}$ corresponds to the spatially infinite system. This line is crossed in the critical point $v = v_{\text{ca}}$ by the curve where below the critical point $\mathrm{Re}\,(\lambda_{L1} - \lambda_{L2}) = 0$ and above the critical point $\mathrm{Im}(\lambda_{L1} - \lambda_{L2}) = 0$. Observe that the eigenvalues are complex for all $k = k_{\text{inf}}$, excluding two points where $\mathrm{Im}\,\lambda_L = 0$. These points fall on either side of the critical point and are located very close to this point.

For the homogeneous inflow boundary condition the solution to the complex GL equation (6) is referred to as a NG mode. A study of this solution was provided by Couairon and Chomaz in [32]. The heteroclinic orbit, representing the NG solution must cross the origin with non-zero U_1 and V_1. As seen from Fig. 7(a) and (b) the orbits with $(k_{\text{inf}}, \omega_{\text{inf}})$ do not satisfy this condition. This means that the presence of the homogeneous boundary condition results in a change of the frequency of the selected solution.

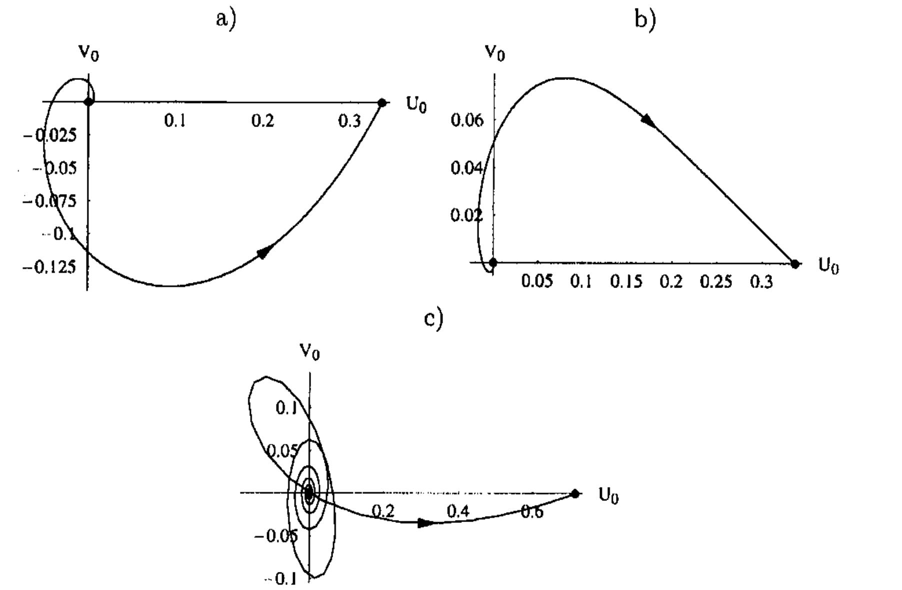

Figure 7. Projections onto the plane (U_0, V_0) of the heteroclinic orbits in the Hopf case for Eq. (29). The parameters are $b_1 = 1$, $c_1 = 1.5$, $b_3 = 1$, $c_3 = 5$, $p = 1$ ($v_{\text{ca}} = 3.601$). In panels (a) and (b) the system is spatially infinite, $k_{\text{inf}} = -0.942$, the instability is convective in panel (a), $v = 7$ ($\omega_{\text{inf}} = -4.697$), and absolute in panel (b), $v = 2$ ($\omega_{\text{inf}} = 0.0121$). In panel (c) the orbit crosses the origin with non zero U_1 and V_1 and hence represents the NG mode, when the homogeneous boundary condition is applied to the inlet, $v = 2$, $k_{\text{NG}} = -0.697$ ($\omega_{\text{NG}} = 1.906$).

To find the NG mode one can trace the heteroclinic solutions to Eq. (29) with different k searching for the simultaneous crossings of zero by U_0 and V_0. As for the infinite mode, there exist a set of NG modes with different phases corresponding to the different points W_N. One such orbit is shown in Fig. 7(c). This orbit leaves the W_L point in a spiraling way. The orbit then makes a loop and its projection returns to the origin of the plane (U_0, V_0), and finally it takes the form of an arc joining the origin (in projection) with one of the W_N points.

On the plane in Fig. 8 we have plotted the line $k = k_{\text{NG}}$. This line represents the wave numbers for the NG mode at different flow rates. Observe that the line ends in the critical point $(k_{\text{inf}}, v_{\text{ca}})$ and that its slope at this point nearly coincides with the curve $\mathrm{Re}\,(\lambda_{L1} - \lambda_{L2}) = 0$.

The problem of frequency selection for the NG mode was studied in [32]. The existence of the NG mode was proved when the corresponding infinite system is absolutely unstable. Moreover, in the critical point the frequency of the NG mode was shown to be the same as for the corresponding infinite mode, i.e., $\omega_{\text{NG}} = \omega_{\text{ca}}$. In the critical point the slope is obtained for the frequency ω_{NG} that is considered as a function of $(p - p_{\text{ca}})$.

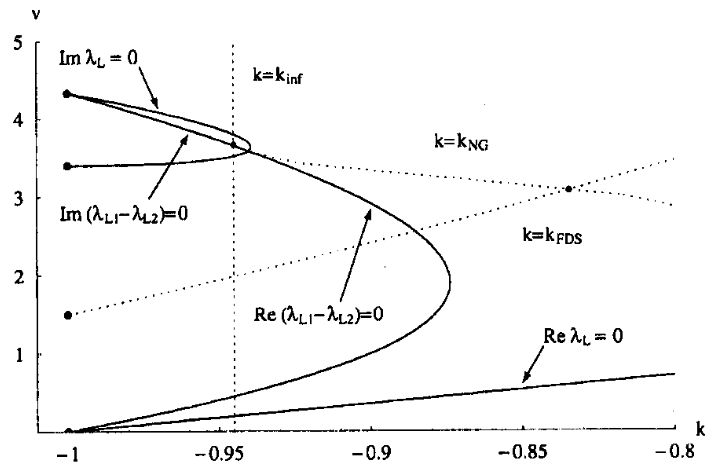

Figure 8. Plane (k, v) of eigenvalues λ_L (40) for the Hopf case. The solid curves represent the roots of Eqs. (41)-(44) while the dashed curves correspond to the different solutions to the GL equation. The parameters are as in Fig. 7. The bullet points on the left edge mark the lower bound of possible values of k as given by Eq. (23). The line $k = k_{\rm inf}$ is crossed in the critical point $v = v_{\rm ca}$ by the curve where below the critical point $\mathrm{Re}(\lambda_{L1} - \lambda_{L2}) = 0$ while above the critical point $\mathrm{Im}(\lambda_{L1} - \lambda_{L2}) = 0$. The curve $k = k_{\rm NG}$ ends in the critical point ($k_{\rm inf}$, $v_{\rm ca}$). Note that the slopes of the curves $k = k_{\rm NG}$ and $\mathrm{Re}(\lambda_{L1} - \lambda_{L2}) = 0$ in the critical point are nearly the same.

Considering the behavior of the curves $k = k_{\rm NG}$ and $\mathrm{Re}(\lambda_{L1} - \lambda_{L2}) = 0$ in Fig. 8, we can suggest a simple estimate for the frequency of the NG mode. Substituting the terms of the equation (43) by their values from (26) and (31) and expressing k via ω using Eq. (22) we can write the approximate equation:

$$\omega_{\rm NG} \approx p\frac{c_1}{b_1} - v^2\frac{c_1}{2(c_1^2 + b_1^2)}. \tag{45}$$

Note that this equation is linear with respect to p and quadratic in terms of v. In the critical point $\omega_{\rm NG} = \omega_{\rm ca}$. In Fig. 9 the exact frequency of the NG mode is compared with that obtained from Eq. (45). We observe that Eq. (45) approximates well the slope of the exact curve in the critical point.

Let us now suppose that an inhomogeneous boundary perturbation is applied to the system inlet. The wave number for the FDS emerging in this case can be obtained from Eq. (22) by substituting $\omega = 0$ and considering condition (23):

$$k_{\rm FDS} = \frac{vb_3 - \sqrt{v^2b_3^2 + 4pc_3(b_1c_3 - c_1b_3)}}{2(b_1c_3 - c_1b_3)}. \tag{46}$$

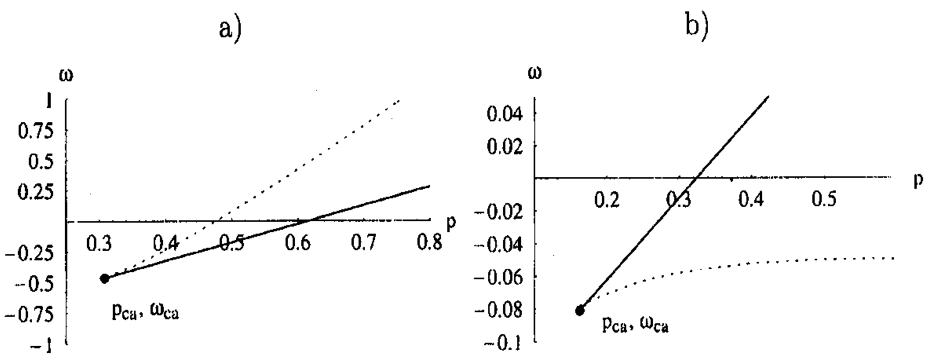

Figure 9. Frequency of the NG mode (dashed line) measured directly from the numerical solution of the GL equation (6) and the approximate frequency obtained from Eq. (45) (solid line). The parameters are (a) $b_1 = 1$, $c_1 = 1.5$, $b_3 = 1$, $c_3 = 5$, $v = 2$; (b) $b_1 = 1$, $c_1 = 0.5$, $b_3 = 1$, $c_3 = -0.2$, $v = 0.9$. Observe, that Eq. (45) approximates well the slope of the exact NG frequency in the critical point while outside of this point the lines diverges.

The graph of this equation is drawn on the plane of Fig. 8. Recall that in Sec. 5 the lower flow rate and the corresponding wave number for which the considered solution exists are found to be $v_{\rm st}$ and $k_{\rm st}$ (19). These vales satisfy Eq. (46).

For the inflow perturbation $w_{x=0} = \rho e^{\varphi}$ the representing heteroclinic orbit must pass through the point ($\rho\cos\varphi$, $\rho\sin\varphi$, 0, 0). In the set of orbits that exist for the given parameters there is only one that satisfies this condition. Hence, the inhomogeneous inflow perturbation defines the phase ϕ of the selected solution.

As we have discussed in Sec. 5, below the critical point, i.e, for $v < v_{\rm ca}$, the system selects one of two solutions depending on the amplitude of the inflow perturbation. If this amplitude is small, an oscillating mode is excited with the same time and space periods as the NG mode. For large perturbations, the flow and diffusion distributed structures gains an advantage in the competition. Unfortunately, the oscillating mode can not be described by Eq. (29) because for $x = 0$ this mode is a nonvanishing constant while the solution of the form (21) permits this only for $\omega = 0$. Hence, the whole picture of competition can not be represented in the phase space of the system (29), and we can only investigate the properties of the heteroclinic orbits for the FDS.

In Fig. 8 the line $k = k_{\rm NG}$ is plotted. This can now be considered as representing the unknown oscillatory solution. The line intersects the line $k = k_{\rm FDS}$. At the point of intersection $\omega = 0$ while at the same time the heteroclinic orbit passes the origin with finite U_1 and V_1. We shall refer to the solution at this point as a stationary NG mode. This solution is illustrated in Fig. 10. In panel (a) the spatio-temporal diagram is presented. Observe that a stationary structure forms for the homogeneous inflow boundary condition. In panel (b) the corresponding heteroclinic orbit is plotted. It has a returning loop and looks like a typical orbit for the NG mode. A remarkable property of this figure is that it remains the same for the inhomogeneous inflow perturbation.

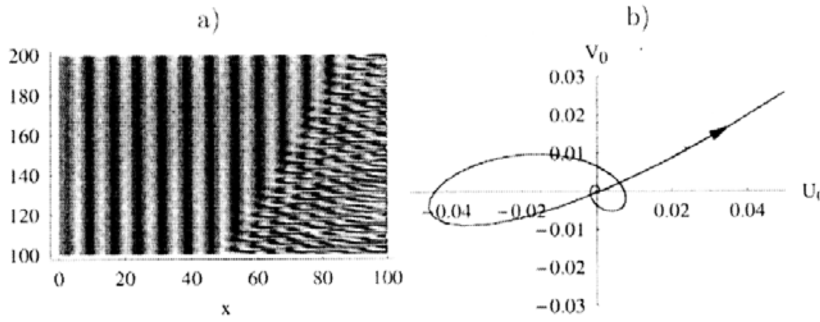

Figure 10. Stationary NG mode for the system (6): Spatio-temporal diagram (a) and the respective heteroclinic orbit (b) obtained when the wave numbers of the FDS and NG mode coincides. The parameters are as in Figs. 7 and 8, the flow rate is $v = 2.9$, and the inflow boundary condition is homogeneous. Note that for the inhomogeneous perturbation this figures would be the same.

The stationary NG mode exist for the GL equation with positive coefficient c_3. As discussed in Sec. 3 in this case the GL equation can describe the slow varying amplitude of the Brusselator model with flow. For negative c_3 the frequency does not cross zero as illustrated in Fig. 9 and, hence no stationary NG mode can be observed.

Competition is absent exactly at the point of the stationary NG mode while outside this point the mode that grows faster in some sense has an advantage. Because in the general case the eigenvalues of the matrix $\mathcal{L}_L$ are complex, a heteroclinic orbit leaves the W_L point in a spiralling way and then assumes the form of an arc. We suppose that the FDS dominates over the oscillating solution when the point of inflow perturbation lies in the FDS orbit on its arc part.

It is convenient to represent the inflow perturbation on the plane (U_0, V_0) as a circle with center at the origin. For the heteroclinic orbit corresponding to the solution with phase ϕ the particular inflow perturbation needed to obtain this solution is defined by the last common point (this can be a point of intersection or touching) of the orbit and the circle.

Let us consider the vicinity of the point of the stationary NG mode. In Figs. 11(a) and (b) the heteroclinic orbits are presented when the system is not very far from this point. We see that the orbits still have the returning loops but they miss the origin. The radii of the circles in these figures are equal to the critical amplitude of perturbation above which the FDS dominates over the oscillating solution (the amplitudes are found from the direct numerical simulations). The critical nature of these circles reveals itself in their geometrical properties. In the last common point the orbit is tangent to the circle. Note that this point lies in the beginning of the arc of the orbit. A small variation of the radius (i.e, the amplitude of perturbation) destroys the picture. Increment transforms the touching into the intersection and decrement result in disappearance of the common point. Thus, in this case we have a clear geometrical criterion for finding the critical amplitude for rigid excitation of FDS.

When the system is far from the point of the stationary NG mode, as in Figs. 11(c) and (d), no definite criteria for the critical amplitude can be found using our approach.

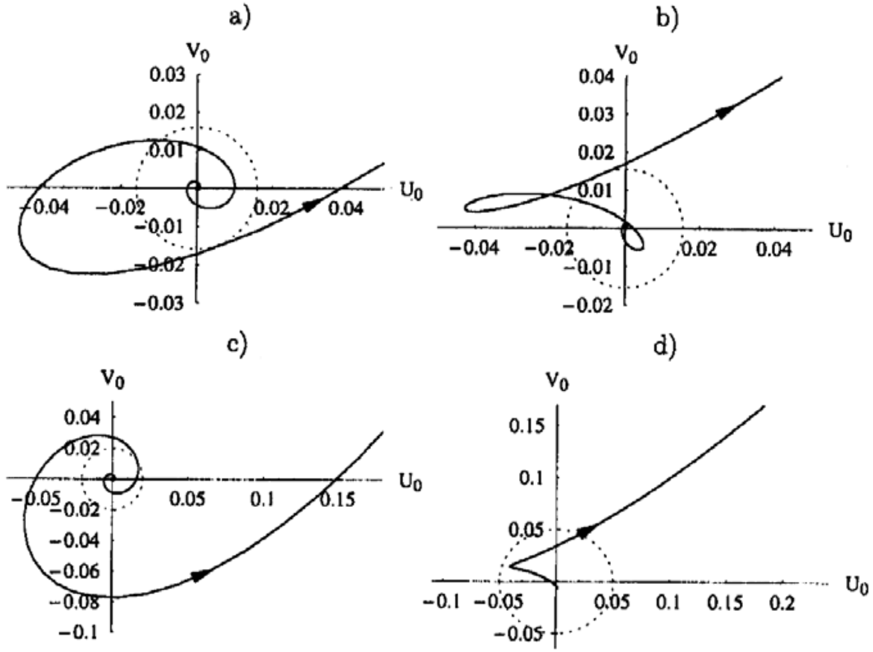

Figure 11. Heteroclinic orbits projected to the plane (U_0, V_0) representing the FDS in the Hopf case. The dashed circles are drawn with the radiuses that are equal to the critical amplitude of the inflow perturbation above which the FDS is excited. The parameters are as in Figs. 7 and 8. The flow rates and the circles radiuses are: (a) $v = 3$, $\rho = 0.016$; (b) $v = 2.8$, $\rho = 0.0155$; (c) $v = 3.4$, $\rho = 0.02$; and (d) $v = 2.7$, $\rho = 0.05$. The flow rates in the panels (a) and (b) are close to the intersection point of the lines $k = k_{FDS}$ and $k = k_{NG}$ on the plane in Fig. 8 and the orbits are tangent to the circles. Two other panels are far from the intersection point and the orbits cross the circles with some angle.

As we see in the figures, the circles for critical perturbation intersect the orbits in points that have no special properties. This is in contrast to the previous case. But our initial suggestion that the FDS dominates if the point of inflow perturbation lies on the arc of the orbit still works. Hence, this can provide a rough estimate for the critical amplitude for which the rigid excitation of flow and diffusion distributed structures takes place.

7. Conclusion

We considered the real and complex Ginzburg-Landau (GL) equations treating them as a weakly nonlinear representation for the one-dimensional Brusselator model with flow near the Turing and Hopf bifurcation thresholds. A real version of the GL equation corresponds to the system near the Turing instability threshold while the complex version corresponds to the Hopf instability. In our analysis we combine the linear approach with numerical calculations of the fully developed time periodic solutions. Some of our results are known as general properties of the GL equation, but we discuss them in the context of the Hopf and Turing instabilities to improve our understanding of the nature of these instabilities.

For both the Hopf and the Turing bifurcations we discussed absolute and convective instabilities in the spatially unlimited system, the appearance of a nonlinear global (NG) mode in the presence of a homogeneous inflow boundary condition, and the emergence of the stationary space periodic solution (flow and diffusion distributed structure, FDS) in the presence of an inhomogeneous constant inflow perturbation.

We found that the FDS can be excited below the critical flow rate if the inflow perturbation is large enough. We refer to this effect as a rigid excitation of FDS. For some parameter values we found the criterion for determination of the critical amplitude of perturbation above which the rigid excitation of FDS takes place.

Finally, we considered the NG modes and found for the complex GL equation an estimate of the frequency for this mode. This estimate was obtained in the linear approach and is valid near the critical point.

Acknowledgments

P.V.K. acknowledges support from CRDF (grant REC-006) and from the Danish Graduate School in Nonlinear Science.

Appendix. Derivation of the Ginzburg-Landau equation for the Brusselator model with flow

Near the bifurcation threshold, distributed systems allow an approximate solution in the form of a fast harmonic wave with an amplitude that is slowly modulated in time and in space. The equation for this slow varying amplitude is called the Ginzburg-Landau (GL) equation [2,3, 41–43]. For a large class of systems, the GL equation takes the form of Eq. (6).

The usual method that one can apply to determine the coefficients of the GL equation for a particular system is the power decomposition of its dynamical variables and parameters with respect to the small bifurcation parameter and the separation of the fast and the slow components.

To perform the decomposition it is important to know the relative scales of variation for all the considered values. This can be found considering that the GL equation is invariant under the rescaling

$$p \to \epsilon^2 p,\ w(x,t) \to \epsilon w(\epsilon x, \epsilon^2 t),\ v \to \epsilon v, \tag{47}$$

where ϵ represents a small scaling factor.

For the following it is convenient to substitute $U \to U_S + U$ and $V \to V_S + V$ into Eq. (1), where U_S and V_S are the steady state (2). The equations for the deviations from the homogeneous steady state then read

$$\begin{aligned} \frac{\partial U}{\partial t} + v\frac{\partial U}{\partial x} - \sigma\frac{\partial^2 U}{\partial x^2} &= (B-1)U + A^2 V + N(U,V), \\ \frac{\partial V}{\partial t} + v\frac{\partial V}{\partial x} - \frac{\partial^2 V}{\partial x^2} &= -BU - A^2 V - N(U,V), \end{aligned} \tag{48}$$

where $N(U, V) = (B/A)U^2 + 2AUV + U^2V$ is the nonlinear term.

The fast component may be found as a solution of the linearized equations (48) at the bifurcation threshold $B = B_H$ or $B = B_T$ and at the rescaled flow rate $v = \epsilon v_1$. For the Hopf and the Turing bifurcations one has

$$\text{Hopf:}\quad \vec{U}_L = \vec{Z}\exp(-i\omega_H t), \tag{49}$$

$$\text{Turing:}\quad \vec{U}_L = \vec{Z}\exp(ik_T x - i\epsilon v_1 k_T t), \tag{50}$$

where $\vec{U}_L \equiv (U_L, V_L)^T$ denotes the solution of the linearized equations (48), ω_H and k_T are given, respectively, by Eqs. (4) and (5), and $\vec{Z} \equiv (Z_U, Z_V)^T$ is the corresponding eigenvector. The norm of this vector determines the amplitude of w and below this is supposed to be normalized as $\vec{Z}/Z_U$.

Now one needs to introduce the new independent time and space variables corresponding to the dynamics on the different scales $\tau_n = \epsilon^n t$ and $\xi_n = \epsilon^n x$ and substitute all the differential operators in Eq. (48) by sums of new operators acting on each new variable separately.

From Eq. (47) we deduce that the slow component w depends on ξ_1 and τ_2. In the Hopf case the fast component depends on t and does not vary in space, see Eq. (49). Hence the sought solution of Eq. (48) depends on t, ξ_1, and τ_2, i.e., $\vec{U} \equiv \vec{U}(t, \xi_1, \tau_2)$, and the differential operators must be substituted by

$$\frac{\partial}{\partial x} \to \epsilon\frac{\partial}{\partial \xi_1},\quad \frac{\partial}{\partial t} \to \frac{\partial}{\partial t} + \epsilon^2\frac{\partial}{\partial \tau_2}. \tag{51}$$

In the Turing case, as follows form Eq. (50), the fast component depends on x and τ_1, i.e., $\vec{U} \equiv \vec{U}(x, \tau_1, \xi_1, \tau_2)$. Hence, the required substitution has the form:

$$\frac{\partial}{\partial x} \to \frac{\partial}{\partial x} + \epsilon\frac{\partial}{\partial \xi_1},\quad \frac{\partial}{\partial t} \to \epsilon\frac{\partial}{\partial \tau_1} + \epsilon^2\frac{\partial}{\partial \tau_2}. \tag{52}$$

Now one can perform the decomposition

$$\vec{U} = \epsilon\vec{U}_1 + \epsilon^2\vec{U}_2 + \epsilon^3\vec{U}_3,\ B = B_{cr} + \epsilon^2 B_2,\ v = \epsilon v_1, \tag{53}$$

and substitute this into Eqs. (48), while accounting also for (51) and (52). Here $\vec{U}_1 = w\vec{U}_L$, and $\vec{U}_2$ and $\vec{U}_3$ are the high order terms. Collecting the identical powers of ϵ and moving in the Turing case the terms

$$\epsilon^{n+1}\left(\frac{\partial \vec{U}_n}{\partial \tau_1} + v_1\frac{\partial \vec{U}_n}{\partial x}\right)\ (n = 1, 2\ldots),$$

from the equation of order $(n+1)$ to the equation of nth order, one obtains the linear equations for $\vec{U}_1$, $\vec{U}_2$ and $\vec{U}_3$. (The additional redistribution of terms is needed to satisfy the solvability condition.) Solving these equations consequently one obtain the GL equation for w, which appears as a solvability condition of the equation for U_3.

References

1. Nicolis, G., and Prigogine, I. 1977, Self-Organization in Nonequilibrium Systems, Wiley, New York.
2. Nicolis, G. 1995, Introduction to Nonlinear Science, Cambridge University Press, Cambridge, England.
3. Walgraef, D. 1997, Spatio-Temporal Pattern Formation, Springer-Verlag, New York.
4. Zhabotinsky, A.M. 1991, Chaos, 1, 379.
5. Guckenheimer, J., and Holmes, P. 1983, Nonlinear Oscillations, Dynamical Systems, and Bifurcations of Vector Fields, Springer-Verlag, New York.
6. Schreiber, I., and Marek, M. 1995, Modelling the Dynamics of Biological Systems: Nonlinear Phenomena and Pattern Formation, E. Mosekilde, and O.G. Mouritsen (Ed.), Springer-Verlag, New York, 23.
7. Ipsen, M., and Schreiber, I. 2000, Chaos, 10, 791.
8. Müller, S.C., Plesser, Th., and Hess, B. 1985, Science, 230, 661.
9. Keener, J.P., and Tyson, J.J. 1986, Physica D, 21, 307.
10. Turing, A.M. 1952, Philos. Trans. R. Soc. B, 237, 37.
11. Castets, V., Dulos, E., Boissonade, J., and De Kepper, P. 1990, Phys. Rev. Lett., 64, 2953.
12. Jensen, O., Pannbacker, V.O., Mosekilde, E., Dewel, G., and Borckmans, P. 1994, Phys. Rev. E, 50, 736.
13. Jensen, O., Mosekilde, E., Borckmans, P., and Dewel, G. 1996, Phys. Scr., 53, 243.
14. Borckmans, P., Jensen, O., Pannbacker, V.O., Mosekilde, E., Dewel, G., and De Wit, A. 1995, Modelling the Dynamics of Biological Systems: Nonlinear Phenomena and Pattern Formation, E. Mosekilde, and O.G. Mouritsen (Ed.), Springer-Verlag, New York, 48.
15. Mosekilde, E., Larsen, F., Dewel, G., and Borckmans, P. 1998, Int. J. Bif. Chaos, 8, 1003.
16. Cross, M.C., and Hohenberg, P.C. 1993, Rev. Mod. Phys., 65, 852.
17. Satnoianu, R.A., Menzinger, M., and Maini, Ph.K. 2000, J. Math. Biol., 41, 493.
18. Landau, L.D., and Lifshitz, E.M. 1959, Fluid Mechanics, Pergamon, Oxford.
19. Briggs, R.J. 1964, Electron Stream Interaction with Plasma, MIT Press, Cambidge, Mass.
20. Bers, A. 1983, Handbook of Plasma Physics, Vol. 1: Basic Plasma Physics, M.N. Rosenbluth, and R.Z. Sagdeev (Ed.), North-Holland, Amsterdam, 451.
21. Lifshitz, E.M., and Pitaevskii, L.P. 1981, Physical Kinetics, Pergamon, London.
22. Michailovsky, A.B. 1975, Theory of Plasma Instabilities (Teorija Plazmennykh Neustoichivostei), Vol. 1, Atomizdat, Moscow.
23. Chomaz, J.M. 1992, Phys. Rev. Lett., 69, 1931.
24. Kuznetsov, S.P., Mosekilde, E., Dewel, G., and Borckmans, P. 1997, J. Chem. Phys., 106, 7609.
25. Kuptsov, P.V., Kuznetsov, S.P., Knudsen, C. 2002, Phys. Lett. A, 294, 210.
26. Dee G., and Langer, J.S. 1983, Phys. Rev. Lett., 50, 383.
27. Dee, G. 1985, J. Stat. Phys., 39, 705.
28. Ben-Jacob, E., Brand, H., Dee, G., Kramer, L., and Langer, J.S. 1985, Physica D, 14, 348.
29. van Saarloos, W. 1988, Phys. Rev. A, 37, 211.
30. van Saarloos, W. 1989, Phys. Rev. A, 39, 6367.
31. Couairon, A., and Chomaz, J.M. 1997, Physica D, 108, 236.
32. Couairon, A., and Chomaz, J.M. 1999, Physica D, 132, 428.

33. Andresén, P., Bache, M., Mosekilde, E., Dewel, G., and Borckmans, P. 1999, Phys. Rev. E, 60, 297.
34. Kærn, M. and Menzinger, M. 1999, Phys. Rev. E, 60, R3471.
35. Andresén, P., Mosekilde, E., Dewel, G., and Borckmans, P. 2000, Phys. Rev. E, 62, 2992. Kærn, M., and Menzinger, M. 2000, Phys. Rev. E, 62, 2994.
36. Satnoianu, R.A., and Menzinger, M. 2000, Phys. Rev. E, 62, 113.
37. Satnoianu, R.A., Maini, P.K., and Menzinger, M. 2001, Physica D, 160, 79.
38. Kærn, M., Menzinger, M., and Hunding, A. 2000, J. Theor. Biol., 207, 473.
39. Kærn, M., Menzinger, M., Satnoianu, R.A., and Hunding, A. 2002, J. R. Chem. Soc., Faraday Discussions, 120, 295.
40. Kærn, M., Satnoianu, R.A., Muñuzuri, A.P., and Menzinger, M. 2002, Phys. Chem. Chem. Phys., in press.
41. Aranson, I.S., and Kramer, L. 2002, Rev. Mod. Phys., 74, 99.
42. Newell, A.C. 1974, Lect. App. Math., 15, 157.
43. Manneville, P. 1990, Dissipative structures and weak turbulence, Academic Press, San Diego.
44. Prigogine, I., and Lefever, R. 1968, J. Chem. Phys., 48, 1965.
45. Hohenberg, P.C., and van Saarloos, W. 1992, Physica D, 56, 303.